communications earth & environment

Article

A Nature Portfolio journal

https://doi.org/10.1038/s43247-025-02449-0

Climate-induced losses of surface water and total water storage in Northeast Asia

Chenchen Zhang [1], Xiangming Xiao [1] ✉, Xinxin Wang [2], Shuang Yi [3], Cheng Meng [1], Yuanwei Qin [1,4], Yuan Yao [1], Leikun Yin [5], Jorge Celis [1], Li Pan [1], Baihong Pan [1], Xuebin Yang [6] & Jinwei Dong [7]

Water shortages are intensifying globally due to climate change and human activities. Northeast Asia, with diverse ecosystems and transboundary water systems, is particularly sensitive to these pressures. Yet, the region's water resource changes and drivers remain largely unknown. Here, we integrate Landsat and Sentinel-2 images, Gravity Recovery and Climate Experiment and its Follow-On observations, climate and anthropogenic data, finding a net surface water area loss of 16×10^3 km^2 in Far East Russia over 2000−2023, primarily driven by rising temperature and evaporative demand, and a net surface water area gain of 3×10^3 km^2 in Northeast China, primarily driven by increasing precipitation and irrigation infrastructure. Approximately 1004 0.5° gridcells (1.4×10^6 km^2) have concurrent losses of surface water area and total water storage. Approximately 185 million people reside in watersheds with surface water area or total water storage loss, underscoring the need for sustainable water management under intensifying climate change and human activities.

Water resources are important for food security, energy production, economics, biodiversity, and human and animal health[1–3]. Both surface water (lakes, rivers, and reservoirs, etc.) and total water storage (TWS) are two of the major metrics for water resources. Surface water is a major component of the TWS[4,5]. Surface water area (SWA) and TWS are strongly interconnected and influenced by many processes, including precipitation, runoff, evapotranspiration, and seepage. Many studies reported that some regions in the world had losses of SWA and/or TWS, for example, the Western United States[6,7], North China[8,9], and the Middle East[10]. Extreme climatic events (floods, droughts) have considerable impacts on SWA and TWS[11,12]. Continued global warming has increased the frequency and severity of extreme climatic events[13], causing devastating impacts on water resources, natural ecosystems, and socio-economics[14].

More than half (52%) of global surface water is found above 44°N latitude of the Northern Hemisphere[15], which includes Northeast Asia (NEA), encompassing Far East Russia, Mongolia, Northeast China, Japan, South Korea, and North Korea. NEA has abundant surface water and large transboundary water systems, which are highly sensitive to human activities and climate change, especially to extreme climatic events[16]. In addition, surface water bodies and nearby wetlands in NEA serve as vital stopover and breeding sites for migratory waterbirds along the East Asia–Australasia Flyway[17], and migratory waterbirds are victims and vectors of highly pathogenic avian influenza (e.g., H5N1)[18]. Moreover, NEA remains relatively understudied in terms of its contribution to the global water cycle[19]. Several local-scale studies reported spatial-temporal dynamics of SWA in the NEA (< 60°N) and explored their drivers[20,21]. A few regional-scale studies reported the spatial-temporal dynamics of SWA and TWS, for example, China[8] and Mongolia[22]. To date, the inter-annual trends and drivers of SWA and TWS in NEA remain poorly quantified, which prevents the community from fully understanding the water resources and implementing effective measures for sustainable water use and management. As NEA is projected to have higher climate warming and more extreme climate events[23], which can amplify the changes of SWA and TWS[24], analyses of SWA and TWS dynamics in NEA are thus critical for understanding the water-climate interaction and feedback.

Most analyses on the spatial-temporal dynamics of surface water used the regional and global surface water datasets that were generated by

[1]School of Biological Sciences, Center for Earth Observation and Modeling, University of Oklahoma, Norman, OK, 73019, USA. [2]Ministry of Education Key Laboratory for Biodiversity Science and Ecological Engineering, National Observations and Research Station for Wetland Ecosystems of the Yangtze Estuary, Institute of Biodiversity Science and Institute of Eco-Chongming, School of Life Sciences, Fudan University, Shanghai, 200438, China. [3]Key Laboratory of Earth System Numerical Modeling and Application, College of Earth and Planetary Sciences, University of Chinese Academy of Sciences, Chinese Academy of Sciences, Beijing, 100049, China. [4]Jiangsu Key Laboratory of Soil and Water Processes in Watershed, College of Geography and Remote Sensing, Hohai University, Nanjing, 211000, China. [5]Department of Bioproducts and Biosystems Engineering, University of Minnesota, St. Paul, MN, 55108, USA. [6]Geography and the Environment Department, Syracuse University, Syracuse, NY, 13244, USA. [7]Key Laboratory of Land Surface Pattern and Simulation, Institute of Geographic Sciences and Natural Resources Research, Chinese Academy of Sciences, Beijing, 100101, China. ✉e-mail: xiangming.xiao@ou.edu

analyzing satellite images, for example, MODIS[25], Landsat[26], and Sentinel-2[27]. However, the use of these data products in NEA often faces several problems associated with the datasets, including moderate spatial resolution[25], infrequent update[15,26], short temporal duration[27], large and irregular gaps in time series data[25], and inaccuracies and uncertainties caused by the datasets used in algorithm training[26]. To date, most of the previous studies on water resources in NEA have been conducted at local or regional scales[22,28], and some of them reported on specific water types, especially on lakes[22,29]. The limited spatial coverage and surface water types could not reflect the overall information on the spatial-temporal dynamics of water resources in NEA.

In this study, we aim to study the spatial-temporal dynamics of SWA and TWS in NEA and investigate how climate change and human activities affect the decadal-scale variability and trends in SWA and TWS. We first use all available Sentinel-2A/B and Landsat 5/7/8/9 imagery and a simple and robust surface water mapping algorithm[6,8,30] to identify surface water in individual images and then calculate annual surface water frequency (SWF) and generate annual yearlong surface water maps (SWF ≥ 0.75). We report SWA calculated from annual yearlong surface water maps in NEA over the period 2000–2023, as Landsat imagery in 1984–1999 could not fully cover NEA (Supplementary Figs. 1, 2). Second, we quantify temporal SWA variations and changes at multiple scales during 2000−2023 and estimate the relative roles of climatic and anthropogenic drivers in determining these variations and trends. Third, we explore the relationship between TWS and SWA, where TWS was derived from the Gravity Recovery and Climate Experiment and its Follow-On (GRACE/GRACE-FO) satellites[31]. We also investigate the impact of extreme climate events (drought, flood) on SWA and TWS by using the Standardized Precipitation Evapotranspiration Index (SPEI) data, which takes into account both precipitation and potential evapotranspiration[32]. Finally, we quantify the number of human populations and their growth living in those areas with SWA and TWS losses at multiple scales.

Results

Annual maps of yearlong surface water at 10 m/30 m spatial resolution during 2000–2023

We generated annual maps of surface water in NEA during 2000−2023 (Supplementary Fig. 3, Supplementary Note 1). Our annual maps of yearlong surface water for 2015–2023 at 10 m spatial resolution and 2000−2014 at 30 m spatial resolution have high accuracies with producer's and user's accuracies of 97% and 98%, respectively, based on validation samples collected in this study, and 91% and 98% using the GLanCE land cover sample dataset (Supplementary Figs. 4, 5).

We cross-compared the annual yearlong surface water layers from our datasets with the 250 m MODIS land/water product (MOD44W) in 2000–2015[25], the 30 m global surface water datasets released by the Joint Research Center (JRC) in 2000–2021[15], the 90 m global OSM Water Layer in 2017[33], and the 10 m ESRI global land cover dataset in 2017–2023[27] (Fig. 1, Supplementary Note 2). At the NEA scale, the SWA from MOD44W dataset was slightly smaller (4% ± 2%) than that from this study (Fig. 1a), which can be attributed to the coarse spatial resolution (250 m) that may fail to identify small surface water bodies covering a limited portion of the pixel (Supplementary Fig. 6a). The SWA from the JRC dataset was 9% ± 2% more than that from this study, particularly for those years after 2013. The SWA from the OSM Water Layer (40%) and the ESRI dataset (30% ± 3%) were much higher than that from our dataset, which can be mainly attributed to the misclassification of seasonal or ephemeral surface water (SWF < 0.75) to yearlong surface water (Supplementary Fig. 6a–c). At the watershed level, the MOD44W and JRC were highly consistent with our dataset with small deviation (slope = 0.96×10^3 and 1.08×10^3 km^2 year^{-1}, R^2 = 0.98 and 0.99, standard error (SE) = 0.004×10^3 and 0.003×10^3 km^2, respectively) (Fig. 1b). The SWA from the OSM Water Layer was in moderate agreement with those in our dataset with a R^2 of 0.56. The SWA from the ESRI dataset was substantially higher than that from our dataset with a slope of 1.20.

Inter-annual variations and changes of SWA across multiple spatial scales

At the NEA scale, the inter-annual trend of SWA in NEA was large, declining from ~204×10^3 km^2 in 2000 to ~188×10^3 km^2 in 2023, a net loss of 16×10^3 km^2 or ~8% of SWA in 2000 (Fig. 2a). Specifically, the inter-annual trends of SWA can be divided into two phases: an insignificant slightly increasing phase between 2000−2010 and a significantly decreasing phase between 2011−2023 (slope = -0.96×10^3 km^2 year^{-1}). At the country/sub-country scale, the inter-annual trends of SWA vary substantially. SWA in Far East Russia accounts for 80% ± 0.3% of the total SWA in NEA and experienced the largest loss, with a ~ 10% decline from 2000−2023 or a net loss of 16×10^3 km^2. SWA in Far East Russia dominated the overall net SWA loss in NEA (Supplementary Fig. 7a), primarily due to its large land area (Supplementary Fig. 7a, b). Mongolia and Japan had significantly decreasing trends of SWA since 2000 with small trends of < 0.1×10^3 km^2 year^{-1}. Northeast China had a significantly moderate increasing SWA trend (0.16×10^3 km^2 year^{-1}), and North Korea had a slightly increasing SWA trend. SWA in South Korea varied a lot over the years with no trend.

At the watershed scale, 37 watersheds (47% of the total of 79 watersheds) had significant SWA loss during 2000−2023, 14 watersheds (18%) had significant SWA gain, and the remaining 28 watersheds (35%) showed no trends (Fig. 2b, c). The SWA gain was mainly found in watersheds along Amur (Heilongjiang), Songhuajiang, and Herlen Rivers, and SWA loss was primarily distributed in most of Far East Russia, west and north Mongolia, and Japan.

At the 0.5° gridcell scale, 2509 gridcells (34% of the total 7321 gridcells) had significantly decreasing SWA trends, whereas 786 gridcells (11%) had significant increasing SWA trends. The remaining 4026 gridcells (55%) showed no trends (Fig. 2d, e). Overall, the high latitudes in NEA had a SWA loss, whereas the polar region (north of 66°33' N) and the mid-latitude region (between 35° N and 55° N) gained SWA during 2000−2023.

Driving factors for inter-annual variations and changes of SWA at 0.5° resolution

Air temperature and PET dominated 64% (33% plus 31%) of the gridcells with SWA loss, whereas precipitation changes contributed 34% (Fig. 3a). Agricultural water infrastructure[34] and increased precipitation mainly contributed to SWA gain in Northeast China (Fig. 3b). Air temperature and PET changes dominated the SWA gain in regions excluding Northeast China.

Overall, the SWA in NEA declined at a net annual rate of -342.6 km^2 year^{-1}, of which air temperature and PET contributed 83% to the decline (Fig. 3c). Within the total rate of -658.5 km^2 year^{-1} in grids with SWA loss, 70% (-461.3 km^2 year^{-1}) is attributable to increasing air temperature and PET (Fig. 3d). Gridcells with SWA loss had lower precipitation trends than the overall average trend, but higher air temperature and PET trends than the overall average trend (Fig. 3f, g). In contrast, a much higher precipitation trend than the overall and SWA loss regions resulted in 40% of the total SWA increasing trend, while a lower warming trend together with a negative PET trend led to 56% of the total increasing trend (Fig. 3e, h). The reservoir construction explained 4% of the total increasing trend (Fig. 3e). In summary, increased air temperature and PET were major reasons for SWA loss, while increased precipitation and agricultural water infrastructure development dominated SWA gain.

Relationships between spatial-temporal changes of SWA and TWS during 2002–2023 across multiple scales

We investigated the spatial-temporal changes of SWA and TWS and their relationship during 2002–2023 in NEA. At the 0.5° grid scale, TWS decreased significantly ($P < 0.05$) in 2629 gridcells (40% of 6555 gridcells) with decline rates from -0.1 cm year^{-1} to -4.1 cm year^{-1}. 896 gridcells (14%) had significantly increasing TWS trends ranging from 0.1 cm year^{-1} to 1.1 cm year^{-1} (Fig. 4a, e). SWA trends during 2002–2023 (Fig. 4b, f) showed similar spatial patterns with those during 2000–2023 (Fig. 2d, e) at 0.5° gridcell scale, with 2006 gridcells (31%) showing a significant decrease with

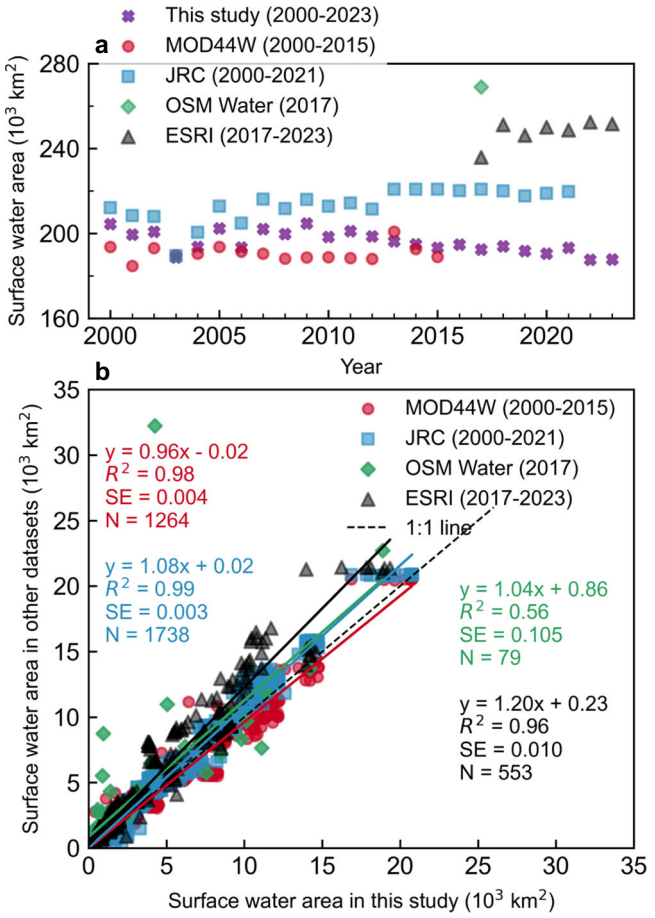

Fig. 1 | Inter-annual dynamics of yearlong surface water area (SWA) in Northeast Asia during 2000−2023. a SWA comparison with other surface water datasets at the Northeast Asia level. **b** SWA comparison with other surface water datasets at the watershed level. SE indicates standard error. Linear regressions used data from the years available for each dataset, i.e., MOD44W (2000−2015), JRC (2000−2021), OSM Water Layer (2017), and ESRI (2017−2023).

rates from -17.2 km^2 year^{-1} to -10.3 m^2 year^{-1}, and 731 gridcells (11%) showing a significant increase with rates from 3.7 m^2 year^{-1} to 12.2 km^2 year^{-1} (Fig. 4b). 1625 gridcells (25%) were experiencing TWS loss (SWA gain or no trend), while 1004 gridcells (15%) experienced both TWS and SWA losses (Fig. 4g). The linear regression models between TWS and SWA showed significant positive correlations in 1245 gridcells (19%) with r-values ≥ 0.4 (Fig. 4c, d, h).

At the watershed scale (a total of 74 watersheds), hotspots of TWS depletion (shown by large declining TWS trends, $P < 0.05$) were found in 32 watersheds in north Far East Russia and south Mongolia with declines ranging from -2.0 to -0.1 cm year^{-1}, and TWS gain was found in 10 watersheds along Amur (Heilongjiang) River and Songhuajiang River and in central Mongolia with rates from 0.2 to 0.7 cm year^{-1} (Fig. 4i, Supplementary Fig. 9a). Significant SWA losses were found in 36 watersheds, which mostly overlap with, but extend beyond, the TWS losses, covering additional areas in watersheds in northeast Far East Russia, west and north Mongolia, and Japan with rates from -163 km^2 year^{-1} to -636 m^2 year^{-1} (Fig. 4j, Supplementary Fig. 9b). SWA gain was mainly found in 12 watersheds along the Amur River and Songhuajiang River with rates from 0.007 km^2 year^{-1} to 157 km^2 year^{-1}. 15 watersheds were experiencing TWS loss (SWA gain or no trend), which raised the concern for excessive groundwater withdrawal due to agricultural irrigation or mining (Supplementary Fig. 9c). 17 watersheds experienced both TWS and SWA losses, posing more serious challenges to the environment and communities. The linear regression models between TWS and SWA showed significant positive correlations ($P < 0.05$) in 20 watersheds (27%) with r-values ≥ 0.5 (Fig. 4k, l, Supplementary Fig. 9d).

We selected three representative watersheds with different SWA trends to study SWA and TWS variations (Fig. 5a). Northeast China is China's important grain production base, and the Songhuajiang River Basin, located in this region, is one of China's seven major river basins[35]. The inter-annual variations of SWA anomalies in the Songhuajiang River Basin reveal distinct cycles of dry and pluvial periods (Fig. 5b), which aligned with documented droughts (2001, 2007, 2011, 2014, 2017) and floods (2005, 2010, 2013, 2020)[36–38]. The first three droughts caused SWA to reach its lowest in 2002, 2008, and 2011, and then recovered to close to the 24 year average in 2006, 2010, and 2012 as SWA gradually increased. The 2014 drought caused SWA to drop largely from 2013, leading to an extended drop in the following years with negative SPEI values. This prolonged impact was further compounded by another drought in 2017, resulting in a continued SWA decline. In contrast to droughts, floods brought large and rapid SWA increases, and aided the recovery of SWA to the average level in 2005 and 2010 with higher precipitation (Supplementary Fig. 10a). The 2013 and 2021 floods, in particular, caused SWA to rise sharply, making it well above the average. TWS followed a similar pattern to SWA, more aligned in later years. This relationship highlights the sensitivity of regional water storage to climatic conditions.

SWA in the Great Lakes Depression in Mongolia declined during 2000−2002 due to La Niña-induced drought, and then recovered in 2003 because of flooding in that year with high positive SPEI (Fig. 5c). SWA in the Great Lakes Depression started to decline substantially from 2003 onwards with a rebound since 2016 and reached the lowest in 2023, suggesting a long-term reduction in SWA in the past two decades. TWS showed a similar decrease with SWA but with larger variations during 2006−2013. Significant SWA and TWS depletions are mainly attributed to exacerbated water loss due to climate change-related temperature warming, reduced precipitation, and intensified drought[22,39] (Supplementary Fig. 10b). In addition, the retreat of snowpack and glaciers in the Altai Mountains caused by rising temperatures has diminished the water inflow to rivers and lakes[40].

SWA in a watershed in the arctic of Far East Russia experienced a slight increase with fluctuation during 2000−2009 as SPEI increased (Fig. 5d). Significantly warmer temperatures led to thermokarst (ground collapse and subsidence) in ice-rich permafrost environments that subsequently filled with water, leading to lake expansion and SWA increase in this phase[41,42]. SWA experienced a significant decrease from 2009 through 2017 as lake water rapidly drained into the subsurface due to thinning and eventual breaching of permafrost near lakes[43–45]. The 2018 extreme flood aided SWA to rapidly recover to average levels. TWS showed a similar pattern with SWA but with larger variations.

Human populations affected by the spatial-temporal changes of SWA and TWS

Water resources are important for human society. In 2020, about 109 million people (32% of the total population in NEA, 338 million) resided in 0.5° gridcells with SWA loss, whereas 63 million (19%) people resided in 0.5° gridcells with TWS loss (Fig. 6a, Supplementary Fig. 11a–c). Given the spatial complexity of water allocation systems and the fact that human water use behavior often extends beyond local water sources near settlements and relies on wider networks of water resources, we further analyzed the relationship between changes in water resources and population at the watershed scale (Supplementary Fig. 11d-f). 140 million (42%) people were living in watersheds with SWA loss. In comparison, 56 million (17%) people were living in watersheds with TWS loss (Fig. 6b). During 2000−2020, the population in NEA had grown by 17 million with a rate of 0.84 million year^{-1}. Among this, it was estimated that there were over half (51%) of the population growth was in gridcells with SWA loss and over one-quarter (26%) in gridcells experiencing both significant SWA and TWS losses (Fig. 6c, Supplementary Fig. 12a–c). 15% of the population growth was found in watersheds with SWA loss, and roughly one-third (31%) in watersheds with TWS loss (Fig. 6d, Supplementary Fig. 12d–f).

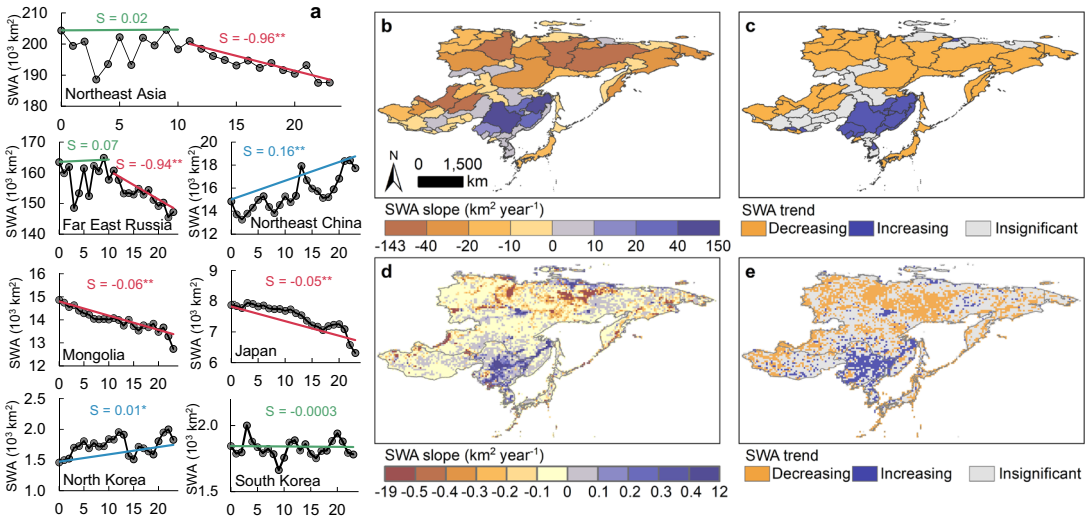

Fig. 2 | Variations and trends of yearlong surface water area (SWA) in Northeast Asia during 2000–2023 across the scales by Northeast Asia, country/sub-country, watershed, and 0.5° gridcell. a Inter-annual changes of SWA for Northeast Asia and each country/sub-country. S indicates Sen's slope, * indicates significant at $P = 0.05$ level, ** indicates significant at $P = 0.001$ level. **b** Inter-annual trends of SWA at the watershed scale (slope values). **c** Inter-annual trends of SWA at the watershed scale. **d** Inter-annual trends of SWA at the 0.5° gridcell scale (slope values). **e** Inter-annual trends of SWA at the 0.5° gridcell scale.

In 2020, densely populated countries/sub-countries, including Japan, Northeast China, and South Korea, had large numbers of people affected by SWA loss and/or TWS loss (Fig. 6e, f). In contrast, sparsely populated countries/sub-countries, including Far East Russia and Mongolia, experienced relatively fewer people impacted by water resource losses. Although North Korea had a large population density, the number of people affected by SWA or TWS loss was comparatively low, as most 0.5° gridcells and watersheds within the country did not show significant water loss. During 2000–2020, Japan, Northeast China, and South Korea experienced substantial population growth in both 0.5° gridcells and watersheds undergoing SWA and/or TWS decline (Fig. 6g, h). This was followed by moderate population increases in Mongolia and North Korea. In contrast, Far East Russia exhibited population decline in regions affected by water resource loss. All estimates involving TWS are conservative because pixels at the sea-land boundary are removed due to leakage errors across coastlines.

Discussion

We used 24-year satellite observations to investigate long-term SWA and TWS dynamics, revealing widespread declines in SWA and TWS in NEA. Prior to this study, SWA and TWS changes in Far East Russia, Japan, and North and South Korea remained poorly understood, as previous studies have mainly focused on water quality rather than water resource availability[46,47]. Our study could provide a basis and insights for water resource changes in these regions.

The resultant yearlong surface water maps of 10 m resolution post-2015 and 30 m resolution pre-2015 in this study provide a robust foundation for capturing fine-scale SWA changes. In regions with complex and fragmented water bodies, finer spatial resolution (10 m) Sentinel-2 data may show slightly more information on the edge of surface water bodies or small-sized surface water bodies (< 30 m) than does 30 m Landsat data. However, for the large spatial scales and annual aggregation used in our analysis, the impact of spatial resolution differences on long-term trend consistency is minimal. Therefore, while some local discrepancies are possible, the overall SWA change trends presented are robust (Supplementary Note 3, Supplementary Fig. 13).

Our findings extend previous knowledge on TWS dynamics[48]. First, we update the assessment period to 2023 by integrating GRACE and GRACE-FO data, thereby extending the work[48] on TWS up to 2016. Extending the observational record is critical for capturing more recent trends, especially under intensifying climate change. Second, in addition to TWS, our study simultaneously analyzes SWA dynamics, a key component of the water cycle that directly influences ecosystem health and biodiversity. Third, our results are complementary to the previous work[48], collectively demonstrating a continuous decline in water resources across high-latitude regions from 2002 to 2023. Together, these contributions provide a more comprehensive and up-to-date understanding of long-term water resource changes in NEA.

Our results reveal consistent losses of SWA and/or TWS across several countries/sub-countries. While Far East Russia exhibited an overall decreasing trend in SWA during 2000–2023, the polar region experienced a SWA increase, aligning with previous studies that reported rising lake water levels[49] and increasing water storage[50]. These findings provide multi-dimensional evidence of water gain in the polar region. SWA in Mongolia has been decreasing since 2000, which was also observed in a study focusing on the SWA in the Mongolian Plateau from 1987 to 2010, despite different water identification methods being applied[22]. Reduced precipitation and drier and warmer climates have been recognized as the major drivers for the SWA decline in Mongolia[22,39], which is consistent with the attribution analysis in our study (Fig. 3a). We found that warmer temperatures and increased PET accounted for 70% of SWA losses, which, together with projected drier and warmer climate[51,52] and resulting increased drought, emphasizes the importance of considering climate change impacts in the management of future surface water resources.

Our results also reveal that climate change and human activities have increased SWA in certain countries/sub-countries. For example, in Northeast China, increased precipitation and agricultural water infrastructure construction dominated the SWA gain[4] (Fig. 3b). This finding is consistent with the previous study which investigated SWA trends across China from 1989 to 2016[8]. When combined with our results extending to 2023, the evidence suggests a continuous increase in SWA in Northeast China since the 1980s. However, some previous studies have reported varying decreases in SWA or TWS in certain lakes and reservoirs[53,54]. As China's largest granary, agricultural development in Northeast China plays an important role in China's social economy, and thus extensive agricultural water infrastructure (irrigation) has been developed. The water resources in Northeast China could be further enriched due to positive SPEI (Fig. 5b) and agricultural structure adjustment in recent years, which has gradually reduced the cultivation area of paddy rice, the most water-consuming crop[55].

While climate-driven factors were identified as the primary drivers of SWA changes across NEA, the influence of human activities may be underestimated, particularly in densely populated countries/sub-countries

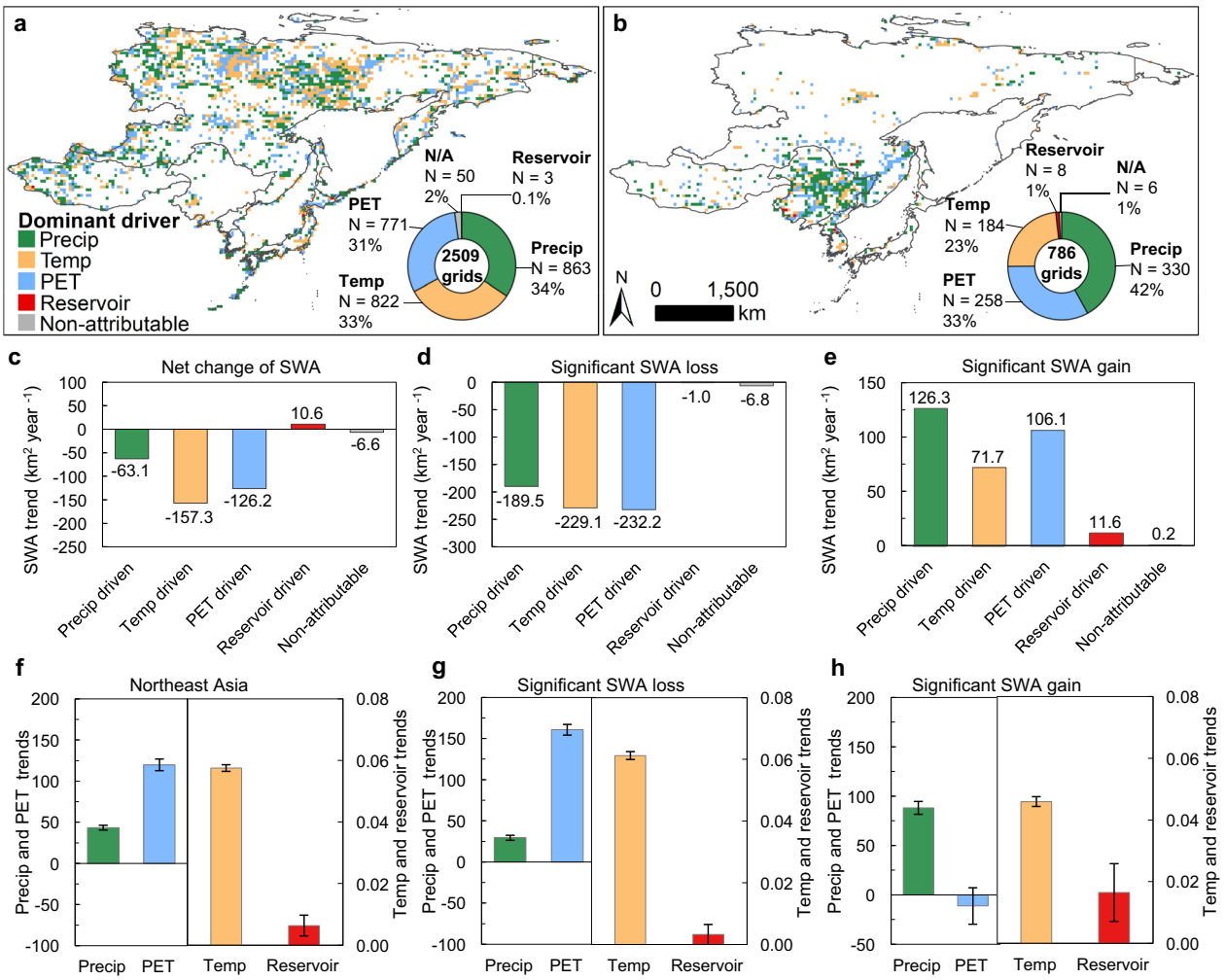

Fig. 3 | Attribution of net change, gross loss, and gross gain of yearlong surface water area (SWA) in Northeast Asia at 0.5° gridcells. a Dominant drivers for SWA loss. **b** Dominant drivers for SWA gain. The insert pie charts in (**a** and **b**) show the proportion of each driver. **c** Trends in SWA net change induced by each driver in Northeast Asia. **d** Trends in SWA loss induced by each driver. **e** Trends in SWA gain induced by each driver. **f** Trends of annual total precipitation (mm year^{-1}), annual total potential evapotranspiration (mm year^{-1}), annual average air temperature (°C year^{-1}), and reservoir area (km^2 year^{-1}) in Northeast Asia. **g** Trends of each predictor in gridcells with SWA loss. **h** Trends of each predictor in gridcells with SWA gain. Error bars represent the trend uncertainties at a 95% confidence interval. Precip, Temp, and PET denote precipitation, air temperature, and potential evapotranspiration, respectively. Note that temperature and PET are highly correlated (Supplementary Fig. 8), but they were plotted separately.

such as Northeast China, Japan, and South Korea. Limited long-term datasets on groundwater use, agricultural practices, and food production across NEA over the full study period (2000–2023)[56–58] constrained our ability to fully quantify anthropogenic impacts. Future studies should incorporate emerging datasets on irrigation, groundwater depletion, and land use change to better separate human and climate influences on water dynamics.

The water system can become vulnerable due to an imbalance in supply and demand, caused by a changing climate and increasing population. The water demand increases with the increasing population growth and concentration, rising temperature[59], and extreme events[60], but the water supply may decrease as a result of climate change (Figs. 3, 5). Regions with large population densities but TWS and/or SWA losses should pay more attention to water source conservation and management. One obvious example is Japan. Even though Japan has constructed many dams and associated reservoirs (Supplementary Fig. 14), SWA still faces significantly decreasing trends (Fig. 2a), which may indicate that the reliability of water supply from reservoirs is decreasing in Japan, presenting challenges to water managers. In addition, climate change has increased the frequency of extreme events[61], posing additional water management challenges[6,8,62]. Given the changing climatic conditions, risk analysis and sustainable water management practices are required to better match available supplies and future demand[63].

Water resource shortage has been becoming more severe worldwide, and land-water systems in NEA are more sensitive to global change and human activities. Our surface water dataset at 30 m/10 m spatial resolution for NEA during 2000−2023 is a reasonably accurate, updated, reliable, and spatially detailed dataset. Temporal SWA dynamics in NEA had a stagnant but varying phase between 2000−2010 and a significantly large decreasing phase between 2011 and 2023, attributed mostly to the large loss in Far East Russia. Increased air temperature and PET are responsible for the SWA loss. Increased precipitation and agricultural water infrastructure dominate SWA gain, as shown by the moderate gain in Northeast China. TWS shows a similar temporal dynamic with SWA but differs in significance. As a large number of people (e.g., 185 million in 2020) reside in those watersheds with SWA or TWS loss, our surface water dataset and the research findings on SWA and TWS dynamics can be used to support data-driven sustainable water management in NEA. The observed SWA/TWS declines, especially in densely populated countries/sub-countries like Japan, Northeast China, and South Korea, highlight growing water stress under climate change and human pressure, emphasizing the need for integrated management strategies that consider both environmental and demographic changes.

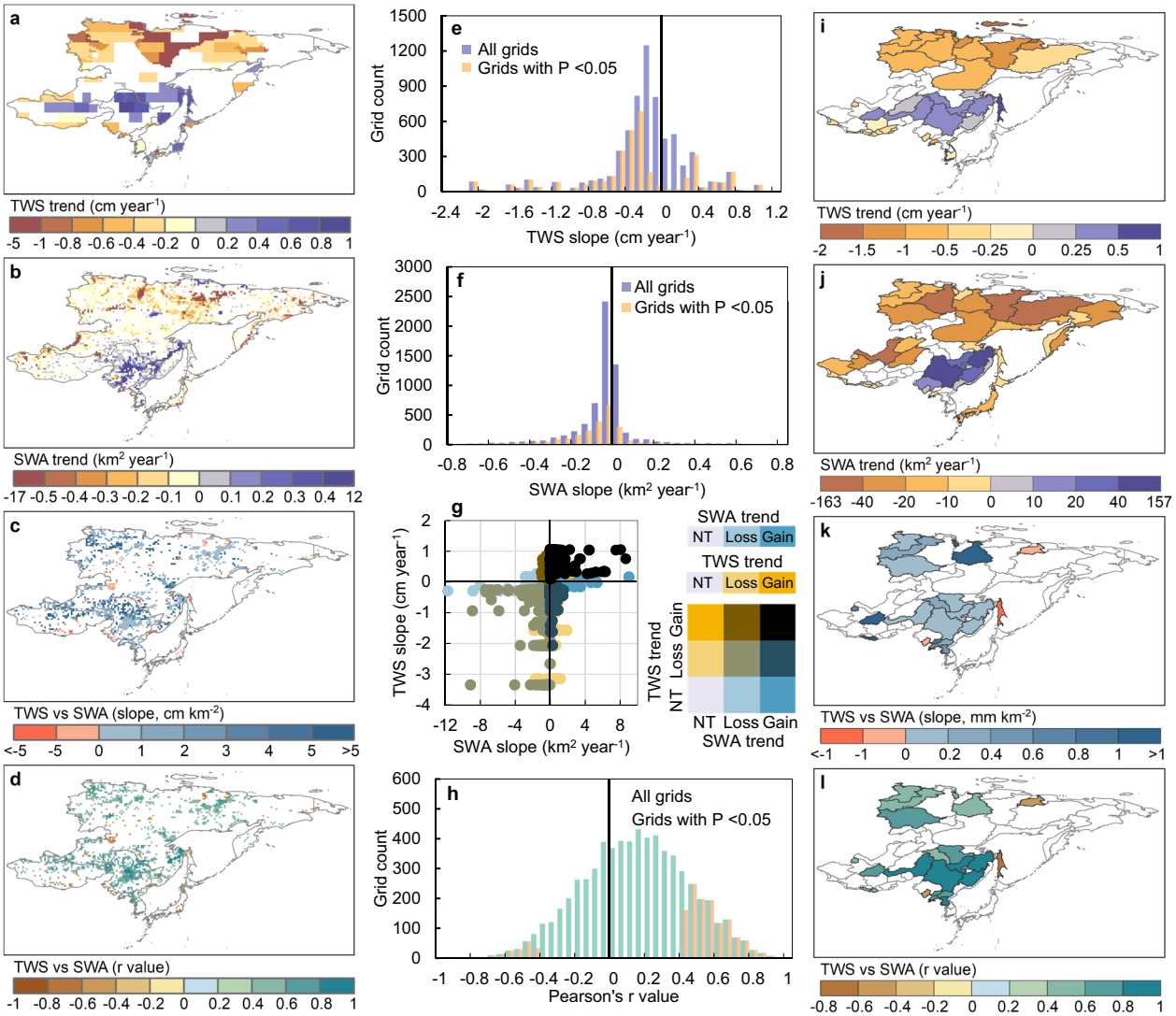

Fig. 4 | Trends of yearlong surface water area (SWA) and total water storage (TWS) and their linear regression at 0.5° gridcell and watershed levels during 2002−2023 with *t*-test at the 5% significance level. a Trends of TWS at the 0.5° gridcell scale. **b** Trends of SWA at the 0.5° gridcell scale. **c** Slopes of linear regression of TWS (dependent variable) over SWA (independent variable) at the 0.5° gridcell scale. **d** *r*-values of linear regression of TWS over SWA at the 0.5° gridcell scale. **e** Distribution of TWS slopes at the 0.5° gridcell scale. **f** Distribution of SWA slopes at the 0.5° gridcell scale. **g** 2-dimension scatterplots of SWA trends and TWS trends at the 0.5° gridcell scale. NT indecates no trend. **h** Distribution of *r*-values at the 0.5° gridcell scale. **i** Trends of TWS at the watershed level. **j** Trends of SWA at the watershed level. **k** Slopes of linear regression of TWS over SWA at the watershed level. **l** *r*-values of linear regression of TWS over SWA at the watershed level.

Methods

Study area

NEA includes 6 countries and sub-country regions: Far East Russia, Mongolia, Northeast China, Japan, South Korea, and North Korea (Supplementary Fig. 15a). NEA covers > 10 million km^2 of land and comprises 338 million (about one-twentieth) of the world population in 2020. Its topography varies substantially, ranging from the mountainous regions (Mongolian Plateau, Stanovoy Range, Verkhoyansk Mountains, Kolyma Mountains, Greater Khingan Mountains) to the immense plains (Northeast China Plain, Kanto Plain) and the coastal regions (Supplementary Fig. 15b). Its climate also varies extensively from the arctic climate in Far East Russia to the temperate climate in Japan. Air temperature varies from extremely cold in the north to warm in the south, and precipitation is relatively low in Far East Russia and Mongolia, moderate in Northeast China and the Korean Peninsula, and high in Japan (Supplementary Fig. 15c, d).

Landsat and Sentinel-2 image data

We acquired all available Landsat 5/7/8/9 surface reflectance (SR) images from January 1, 1984, to December 31, 2023, in NEA (~ 592,000 images) in the Google Earth Engine (GEE) platform. Observations with cirrus, clouds, and cloud shadows were identified as bad-quality observations by using the observation quality attributes (QA_PIXEL band) generated from the CFMASK algorithm. Observations with snow/ice were also identified by using the criteria that $SR_{near\text{-}infrared}$ >0.11 and normalized difference snow index (NDSI) > 0.4. The Copernicus 30 m Digital Elevation Model data (GLO-30), along with the solar azimuth and zenith angles of each Landsat image, were used to identify those pixels with terrain shadows[6,8]. The resultant bad-quality, snow-affected, and terrain-shadow observations were then excluded from data analyses for identifying surface water.

We also acquired Sentinel-2A/B SR data for 2019–2023 (~ 1,506,000 images) and top of atmosphere (TOA) data for 2015–2018 (~ 558,000 images) in NEA (note that no SR data were available prior to 2019 in NEA at the time we did image data analyses). Bands of QA60 bitmask band, Sentinel-2 associated Cloud Probability Collection (S2_CLOUD_PROBABILITY), blue band (SR_{blue} > 0.2), and Scene Classification (SLC) band were integrated to identify clouds, cloud shadows, and cirrus in the SR images. QA60 bitmask band, Cloud Probability Collection, and blue

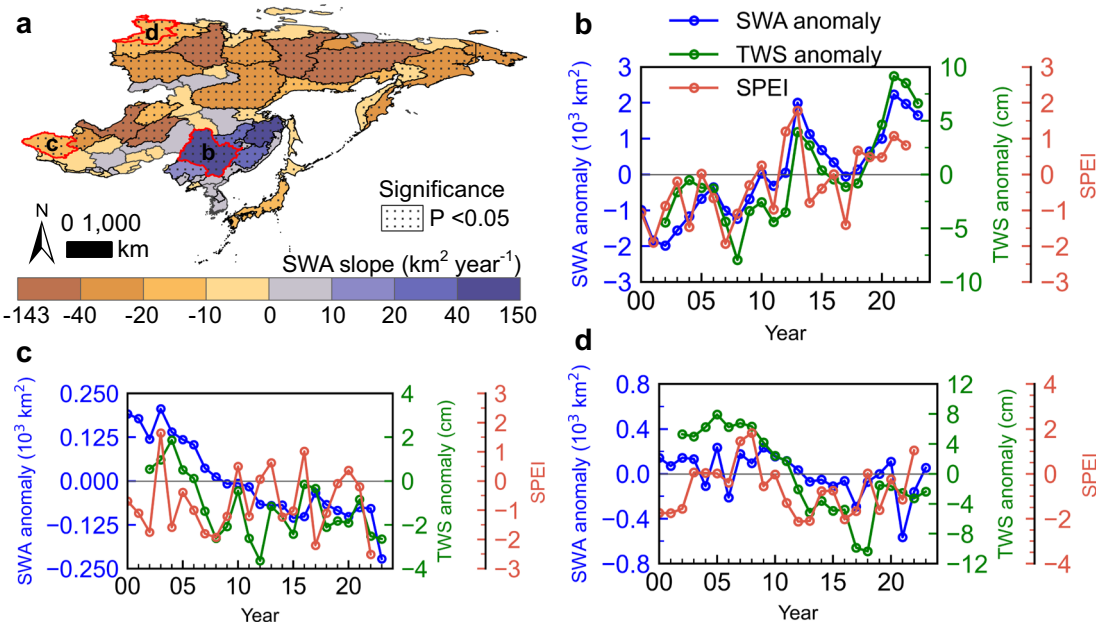

Fig. 5 | Yearlong surface water area (SWA), total water storage (TWS), and the standardized precipitation-evapotranspiration index (SPEI) at the watershed scale. a Distribution of the selected watersheds, background is SWA trend slopes during 2000–2023. **b**-**d** Time series SWA anomaly, TWS anomaly, and SPEI for (**b**) Songhuajiang River Basin in Northeast China, (**c**) Great Lakes Depression in Mongolia, and (**d**) a watershed in the Arctic in Far East Russia.

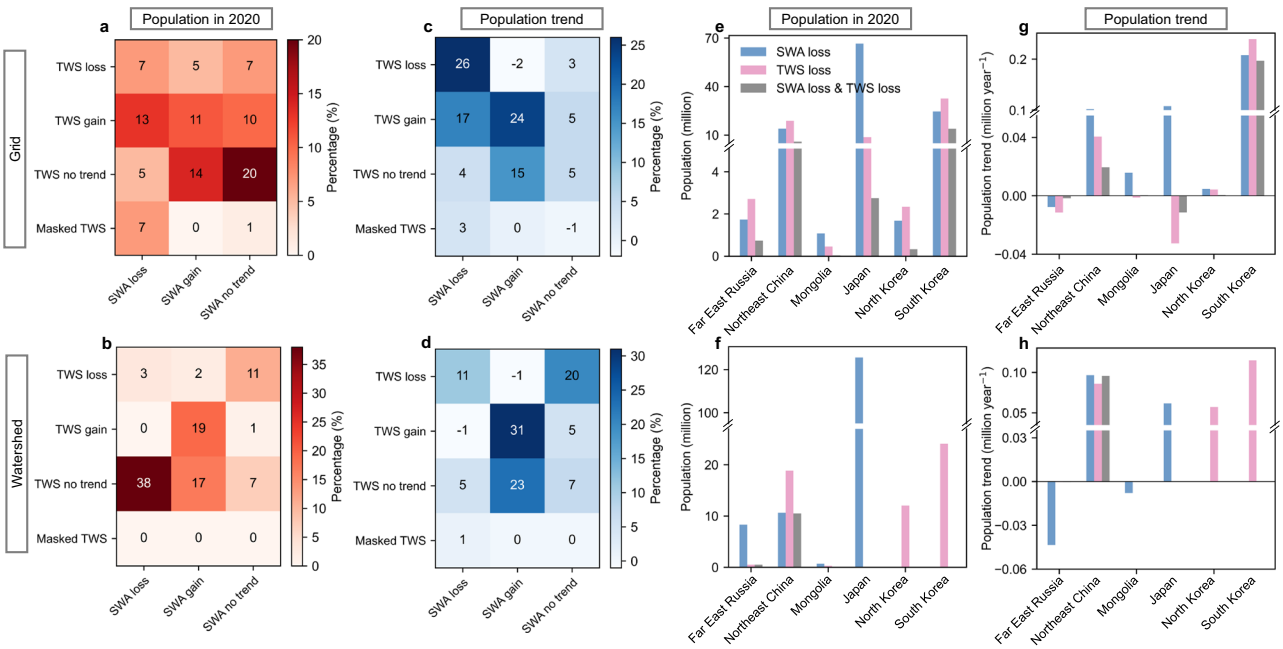

Fig. 6 | Percentages of population and their trend in Northeast Asia with different water resource conditions. a, **b** Percentages of population in Northeast Asia in 2020 residing in (**a**) 0.5° gridcells and (**b**) watersheds with different surface water area (SWA) and total water storage (TWS) trend conditions. **c**, **d** Percentages of population trends during 2000–2020 in (**c**) 0.5° gridcells and (**d**) watersheds with different SWA and TWS trend conditions. **e**, **f** Population in 2020 affected by SWA loss and/or TWS loss in each country/sub-country summarized by (**e**) 0.5° gridcells and (**f**) watersheds. **g**, **h** Population trend in (**g**) 0.5° gridcells and (**h**) watersheds with SWA loss and/or TWS loss in each country/sub-country.

band were used to identify clouds and cirrus in the TOA images, as the SLC band is not available in Sentinel-2 TOA images. Observations affected by snow/ice and terrain shadows in Sentinel-2 images were identified by the same algorithms applied in Landsat images. The bad-quality, snow-affected, and terrain-shadow observations were then excluded from data analyses for identifying surface water.

The availability of Landsat and Sentinel-2 images varies in space and time (Supplementary Figs. 1, 2). We analyzed all the images for 1984—2023. As large proportions of NEA were not covered fully with Landsat images during 1984—1999, in this study we only reported the results for the entire NEA over 2000—2023.

Normalized difference vegetation index (NDVI), enhanced vegetation index (EVI), and modified normalized difference water index (mNDWI)

were calculated for individual good-quality observations using Eqs. (1)–(3).

$$\mathrm{NDVI} = \frac{NIR - Red}{NIR + Red} \tag{1}$$

$$\mathrm{EVI} = 2.5 \times \frac{NIR - Red}{NIR + 6Red - 7.5Blue + 1} \tag{2}$$

$$\mathrm{mNDWI} = \frac{Green - SWIR}{Green + SWIR} \tag{3}$$

where *Blue*, *Green*, *Red*, *NIR*, and *SWIR* are values of blue, green, red, near-infrared, and shortwave-infrared bands for Landsat and Sentinel-2 images.

Total water storage (TWS) data

The Gravity Recovery and Climate Experiment (GRACE) and its follow-on (GRACE-FO) GRCTellus JPL Mascon products (RL06.1Mv03)[31] were used to measure and monitor total water storage (TWS) during 2002–2023. GRACE/GRACE-FO missions provide monthly liquid water equivalent thickness (LWET) anomalies relative to the 2004.0-2009.999 time-mean baseline, which represents the deviations of mass in terms of the vertical extent of water in centimeters. The datasets have a spatial resolution of 0.5° by 0.5° (latitude and longitude). Missing epochs in GRACE/GRACE-FO were filled using the Singular Spectrum Analysis (SSA) gap-filling method[64], which handles time series data with missing samples by exploiting the temporal correlation of the available ones. LAND_MASK.CRI file was applied to mask out the ocean pixels to avoid leakage errors across coastlines. The gap-filled monthly LWET data during 2002–2023 were then used to calculate annual average TWS, which were used to explore trends and their relationship with SWA over the same period.

We also calculated the annual average TWS without gap-filling and compared TWS trends with and without gap-filled data to quantify the impacts of gap-filling (Supplementary Note 4, Supplementary Fig. 16).

Climate data

The Standardized Precipitation Evapotranspiration Index (SPEI) was designed to consider both precipitation and potential evapotranspiration and can capture the major impacts of increased temperatures on water demand. The 12 month accumulative SPEI (the sum of the SPEI for December and the previous 11 months) during 2000−2022 was acquired from the global 0.5° SPEI database (SPEIbase) v2.9[32] to investigate the effect of climate change on SWA and TWS in NEA at the watershed scale.

0.1° daily accumulated precipitation (liquid and frozen water, including rain and snow) and 2 m air temperature were derived from fifth-generation reanalysis (ERA5-Land) daily aggregated data from the European Center for Medium-Range Weather Forecasts (ECMWF) to calculate the annual total precipitation and annual average temperature during 2000–2023, which were used as predictor variables in the ridge regression models for inter-annual variations of SWA in NEA.

Monthly potential evapotranspiration (PET) data were acquired from the TerraClimate datasets[65]. We calculated the annual total PET during 2000−2023.

Reservoir data

Reservoir data were acquired from the Global Dam Watch (GDW) database v1.0[66]. There were 1225 reservoirs in NEA, and 869 of them had the information on construction year (Supplementary Fig. 14). We calculated the reservoir area for each year to explore its contribution to the changes of SWA at the 0.5° gridcell scale during 2001−2022.

Human population data

We acquired 30 arc-second (~ 1 km) human population data for the years 2000, 2005, 2010, 2015, and 2020 from the Gridded Population of World Version 4 Revision 11 (GPWv4.11)[67]. This dataset contains estimates of the number of persons per square kilometer consistent with national censuses and population registers.

Surface water body identification algorithm

In this study we used the mNDWI/VIs-based surface water detection algorithm, defined as [water = (mNDWI > NDVI or mNDWI > EVI) and (EVI < 0.1)][6,68], to detect and map surface water bodies in NEA, which has already been implemented to study surface water changes in the state of Oklahoma, US[30], the contiguous United States[6], and China[8] with high accuracy. The surface water body was first identified using the mNDWI/VIs algorithm in individual pixels of each image in a single year, and then we calculated the annual surface water frequency (SWF) for each pixel for 2000−2023, respectively. SWF, ranging from 0 to 1, is the ratio of the number of surface water body observations to the number of good-quality observations in a year. For each year, water pixels with SWF ≥ 0.75 were defined as yearlong surface water bodies[6,68]. Landsat images were used to generate surface water maps for 2000–2014 with a spatial resolution of 30 m, and Landsat and Sentinel-2 images were integrated to generate surface water maps for 2015−2023 with a spatial resolution of 10 m as Sentinel-2 imagery has been available since 2015 onwards. The Landsat images since 2015 were resampled to 10 m using the nearest neighbor method to be spatially consistent with the Sentinel-2 images.

Accuracy assessment of surface water body maps

The stratified random sampling approach was used to collect validation sample points for the accuracy assessment of our yearlong surface water maps. Referring to the validation strategy of the Joint Research Center (JRC) surface water dataset[15] which considered the small spatial extent of inland water surfaces and its intrinsic spatial-temporal variability, we collected one reference dataset to estimate the producer's accuracy (PA, the measure of omission error) and one to estimate the user's accuracy (UA, the measure of commission error). To generate the sample collection for PA estimation, we first divided NEA into 7321 gridcells (0.5° × 0.5°). Using the 2000 global 30 m inland water body dataset (GLCF)[69] as the reference surface water map to indicate areas with a high probability of surface water occurrence, a potential yearlong surface water point was randomly selected within the GLCF layer in each gridcell. We randomly assigned each point a year of 2000−2023 and then visually examined the time series of Landsat/Sentinel-2 imagery in GEE and very high spatial resolution (VHSR) imagery in Google Earth for that year, only points with confirmed year-round presences of water were used to estimate the PA of yearlong surface water.

To generate UA estimation samples, we first assigned a random year of 2000−2023 for each gridcell. For each gridcell, the yearlong surface water map generated using our mNDWI/VIs algorithm for that year was used as the reference map, and a point was randomly generated within the surface water map. The year-round presence of surface water for each point in the assigned year was visually checked by the time series of Landsat/Sentinel-2 and Google Earth VHSR imagery. Finally, 4424 samples were collected for PA estimates and 6680 samples for UA estimates (Supplementary Fig. 4).

Cross-comparison with other surface water datasets

Surface water thematic datasets and surface water layers from the global land cover products were used for cross-comparison with our yearlong surface water dataset in terms of accuracy, area, and spatial distribution (Supplementary Note 2, Supplementary Figs. 5, 6). We acquired the MODIS land/water mask 250 m product (MOD44W V6)[25] which is derived using a decision tree classifier trained with MODIS data and is available for 2000-2015. We also acquired the permanent water layers from the 30 m global surface water datasets released by the JRC from 2000 to 2021[15], which were generated using Landsat 5/7/8 images. The global 90 m OSM Water Layer[33] was generated by extracting surface water features from OpenStreetMap (OSM) as of January 2018, so its area was compared with our 2017 water map. Yearlong surface water layers from ESRI 10 m global land cover for 2017−2023[27] were collected, which were generated through 10 m Sentinel-2

annual scene collections, billions of human-labeled pixels, and deep learning models.

We conducted accuracy assessments for the yearlong surface water maps from this study, MOD44W, JRC, OSM water layer, and ESRI land cover maps, using both manually collected validation samples and the global land cover sample dataset (GLanCE)[70] (Supplementary Note 2, Supplementary Fig. 5).

Statistical analyses

Yearlong SWA was calculated based on the annual yearlong surface water maps during 2000−2023 for each 0.5° gridcell, watershed, country/subcountry, and entire NEA. The SWA trends during 2000−2023 and 2002−2023 and TWS trends during 2002−2023 were analyzed using the Mann-Kendall test with a confidence level of 95%. The relationships between TWS and SWA at 0.5° gridcell and watershed scales were calculated and analyzed through linear regression with a *t*-test at the 5% significance level.

Ridge regression was conducted to quantify the contribution of the potential climatic and anthropogenic predictors to SWA changes during 2001−2022. We constructed the ridge regression model between annual SWA change and climatic (annual total precipitation, annual average temperature, and annual total potential evapotranspiration) and anthropogenic (reservoir area) predictors for 0.5° gridcells. The annual SWA change was calculated as the difference between the SWA in the current year and that in the previous year. The relative contribution of each driver was calculated as the absolute value of the standard ridge regression coefficient for each factor divided by the sum of the absolute values of all standardized regression coefficients for all drivers. The dominant driver was defined as the driver with the largest relative contribution, which explains the most variation in SWA changes. The contribution of each driver to SWA changes is calculated by multiplying the slope of the SWA trend by its relative contribution. We summarized the contribution of each driver in gridcells with significant SWA trends. Before performing ridge regression, all independent variables were Z-score normalized to facilitate comparison between independent variables of different units and magnitudes.

Data availability

The annual yearlong surface water maps[71] can be accessed at Figshare. Landsat images, including Landsat 5 Thematic Mapper, Landsat 7 Enhanced Thematic Mapper-plus, Landsat 8 Operational Land Imager, and Landsat 9 Operational Land Imager 2, are available from the US Geological Survey at http://earthexplorer.usgs.gov. Sentinel-2 images, including Sentinel-2A and Sentinel-2B, are available from the Copernicus Data Space Ecosystem at https://dataspace.copernicus.eu/. The GRACE and its follow-on (GRACE-FO) GRCTellus JPL Mascon products (RL06.1Mv03) can be downloaded from NASA Jet Propulsion Laboratory (JPL) at https://grace.jpl.nasa.gov/. The Standardized Precipitation Evapotranspiration Index (SPEI) dataset is available from http://sac.csic.es/spei/. The ECMWF fifth-generation reanalysis (ERA5-Land) daily aggregated data are available at https://developers.google.com/earth-engine/datasets/catalog/ECMWF_ERA5_LAND_DAILY_AGGR. The TerraClimate dataset is available from Climatology Lab at https://www.climatologylab.org/terraclimate.html. The Global Dam Watch (GDW) database v1.0 is available at https://www.globaldamwatch.org. The Gridded Population of World Version 4 Revision 11 (GPWv4.11) can be downloaded from https://sedac.ciesin.columbia.edu/data/collection/gpw-v4. All the data except the GDW dataset are also available from the Google Earth Engine platform at https://earthengine.google.com.

Received: 7 February 2025; Accepted: 5 June 2025;
Published online: 19 June 2025

References

1. Brown, C. & Lall, U. Water and economic development: The role of variability and a framework for resilience. *Nat. Resour. forum.* **30**, 306–317 (2006).
2. Ahrens, A. K., Selinka, H.-C., Mettenleiter, T. C., Beer, M. & Harder, T. C. Exploring surface water as a transmission medium of avian influenza viruses–systematic infection studies in mallards. *Emerg. Microbes Infect.* **11**, 1250–1261 (2022).
3. Holgerson, M. A. & Raymond, P. A. Large contribution to inland water CO2 and CH4 emissions from very small ponds. *Nat. Geosci.* **9**, 222–226 (2016).
4. Tao, S. et al. Changes in China's water resources in the early 21st century. *Front. Ecol. Environ.* **18**, 188–193 (2020).
5. Getirana, A., Kumar, S., Girotto, M. & Rodell, M. Rivers and floodplains as key components of global terrestrial water storage variability. *Geophys. Res. Lett.* **44**, 10,359–310,368 (2017).
6. Zou, Z. et al. Divergent trends of open-surface water body area in the contiguous United States from 1984 to 2016. *Proc. Natl Acad. Sci. USA* **115**, 3810–3815 (2018).
7. Averyt, K. et al. Sectoral contributions to surface water stress in the coterminous United States. *Environ. Res. Lett.* **8**, 035046 (2013).
8. Wang, X. et al. Gainers and losers of surface and terrestrial water resources in China during 1989–2016. *Nat. Commun.* **11**, 1–12 (2020).
9. Feng, W. et al. Evaluation of groundwater depletion in North China using the Gravity Recovery and Climate Experiment (GRACE) data and ground-based measurements. *Water Resour. Res.* **49**, 2110–2118 (2013).
10. Khaki, M. & Hoteit, I. Monitoring water storage decline over the Middle East. *J. Hydrol.* **603**, 127166 (2021).
11. Huang, L., Zhou, P., Cheng, L. & Liu, Z. Dynamic drought recovery patterns over the Yangtze River Basin. *Catena* **201**, 105194 (2021).
12. Smith, A. B. & Katz, R. W. US billion-dollar weather and climate disasters: data sources, trends, accuracy and biases. *Nat. Hazards* **67**, 387–410 (2013).
13. Lee, H. et al. *IPCC, 2023: Climate Change 2023: Synthesis Report, Summary for Policymakers. Contribution of Working Groups I, II and III to the Sixth Assessment Report of the Intergovernmental Panel on Climate Change* (Core Writing Team, Lee, H. & Romero, J.) 1−34 (IPCC, Geneva, 2023).
14. Koncagül, E., Connor, R. & Abete, V. *The United Nations World Water Development Report 2024: Water For Prosperity And Peace*, Vol. **153** (UNESCO Digital Library, 2024).
15. Pekel, J.-F., Cottam, A., Gorelick, N. & Belward, A. S. High-resolution mapping of global surface water and its long-term changes. *Nature* **540**, 418–422 (2016).
16. Ha, K.-J., Kam, J., Watanabe, M., Zhou, T. & Dong, W. Grand Challenges in Earth Science: The Weather–Climate–Society Nexus over Northeast Asia. *Bull. Am. Meteorol. Soc.* **104**, E1956–E1961 (2023).
17. Yi, K. et al. Using tracking data to identify gaps in knowledge and conservation of the critically endangered Siberian crane (Leucogeranus leucogeranus). *Remote Sensing* **14**, 5101 (2022).
18. Newman, S. H. et al. Migration of whooper swans and outbreaks of highly pathogenic avian influenza H5N1 virus in eastern Asia. *PLoS ONE* **4**, e5729 (2009).
19. Sogno, P., Klein, I. & Kuenzer, C. Remote sensing of surface water dynamics in the context of global change—a review. *Remote Sens.* **14**, 2475 (2022).
20. Ohba, M., Arai, R., Sato, T., Imamura, M. & Toyoda, Y. Projected future changes in water availability and dry spells in Japan: Dynamic and thermodynamic climate impacts. *Weather Clim. Extremes* **38**, 100523 (2022).
21. Zhang, X. et al. Understanding the shift in drivers of terrestrial water storage decline in the central Inner Mongolian steppe over the past two decades. *J. Hydrol.* **636**, 131312 (2024).
22. Tao, S. et al. Rapid loss of lakes on the Mongolian Plateau. *Proc. Natl Acad. Sci. USA* **112**, 2281–2286 (2015).
23. Sun, X. et al. Asian climate warming since 1901: observation and simulation. *Clim. Res.* **91**, 67–82 (2023).

24. Park, H. et al. Quantification of warming climate-induced changes in terrestrial Arctic river ice thickness and phenology. *J. Clim.* **29**, 1733–1754 (2016).
25. Carroll, M. et al. MOD44W: Global MODIS water maps user guide. *Int. J. Digit. Earth* **10**, 207–218 (2017).
26. Pickens, A. H. et al. Mapping and sampling to characterize global inland water dynamics from 1999 to 2018 with full Landsat time-series. *Remote Sens. Environ.* **243**, 111792 (2020).
27. Karra, K. et al. Global land use/land cover with Sentinel 2 and deep learning. In *2021 IEEE International Geoscience and Remote Sensing Symposium IGARSS*. 4704−4707 (IEEE, 2021).
28. Kim, D. et al. Monitoring river basin development and variation in water resources in transboundary Imjin River in North and South Korea using remote sensing. *Remote Sens.* **12**, 195 (2020).
29. Sumiya, E. et al. Changes in water surface area of the lake in the Steppe region of Mongolia: a case study of Ugii Nuur Lake, Central Mongolia. *Water* **12**, 1470 (2020).
30. Zou, Z. et al. Continued decrease of open surface water body area in Oklahoma during 1984–2015. *Sci. Total Environ.* **595**, 451–460 (2017).
31. Landerer, F. W. et al. Extending the global mass change data record: GRACE follow-on instrument and science data performance. *Geophys. Res.Lett.* **47**, e2020GL088306 (2020).
32. Vicente-Serrano, S. M., Beguería, S. & López-Moreno, J. I. A multiscalar drought index sensitive to global warming: the standardized precipitation evapotranspiration index. *J. Clim.* **23**, 1696–1718 (2010).
33. Yamazaki, D. et al. MERIT Hydro: A high-resolution global hydrography map based on latest topography dataset. *Water Resour. Res.* **55**, 5053–5073 (2019).
34. Xinhua News Agency. *Building An Efficient Water-saving Irrigation Network In Northeast China's Grain-producing Region Holds Promise For Reducing Reliance On Rainfall-dependent Agriculture*. https://www.gov.cn/jrzg/2011-11/07/content_1987695.htm. (2011).
35. Li, X., Wellen, C., Liu, G., Wang, Y. & Wang, Z.-L. Estimation of nutrient sources and transport using Spatially Referenced Regressions on Watershed Attributes: a case study in Songhuajiang River Basin, China. *Environ.l Sci. Poll. Res.* **22**, 6989–7001 (2015).
36. Gao, J. & Gao, H. Influence of the northeast cold vortex on flooding in Northeast China in summer 2013. *J. Meteorol. Res.* **32**, 172–180 (2018).
37. Wang, H. & He, S. The north China/northeastern Asia severe summer drought in 2014. *J. Clim.* **28**, 6667–6681 (2015).
38. Chen, X., Jiang, J. & Li, H. Drought and flood monitoring of the Liao River Basin in Northeast China using extended GRACE data. *Remote Sens.***10**, 1168 (2018).
39. Kang, S., Lee, G., Togtokh, C. & Jang, K. Characterizing regional precipitation-driven lake area change in Mongolia. *J. Arid Land* **7**, 146–158 (2015).
40. Pan, C. G. et al. Glacier recession in the Altai Mountains of Mongolia in 1990–2016. *Geografiska Annaler Series A Phys. Geogr.* **100**, 185–203 (2018).
41. Kokelj, S. V. & Jorgenson, M. Advances in thermokarst research. *Permafrost and Periglacial Processes* **24**, 108–119 (2013).
42. Veremeeva, A., Nitze, I., Günther, F., Grosse, G. & Rivkina, E. Geomorphological and climatic drivers of thermokarst lake area increase trend (1999–2018) in the Kolyma lowland yedoma region, north-eastern Siberia. *Remote Sens.* **13**, 178 (2021).
43. Smith, L. C., Sheng, Y., MacDonald, G. & Hinzman, L. Disappearing arctic lakes. *Science* **308**, 1429–1429 (2005).
44. Webb, E. E. et al. Permafrost thaw drives surface water decline across lake-rich regions of the Arctic. *Nat.Clim. Change* **12**, 841–846 (2022).
45. Liu, A., Chen, Y. & Cheng, X. Monitoring thermokarst Lake Drainage dynamics in northeast siberian coastal tundra. *Remote Sens.* **15**, 4396 (2023).
46. Fan, M. & Shibata, H. Simulation of watershed hydrology and stream water quality under land use and climate change scenarios in Teshio River watershed, northern Japan. *Ecol. Indicators* **50**, 79–89 (2015).
47. Mainali, J. & Chang, H. Landscape and anthropogenic factors affecting spatial patterns of water quality trends in a large river basin, South Korea. *J. Hydrol.* **564**, 26–40 (2018).
48. Rodell, M. et al. Emerging trends in global freshwater availability. *Nature* **557**, 651–659 (2018).
49. Xu, N. et al. Satellite observed recent rising water levels of global lakes and reservoirs. *Environ. Res. Lett.* **17**, 074013 (2022).
50. Xu, N., Li, W., Gong, P. & Lu, H. Satellite altimeter observed surface water increase across lake-rich regions of the Arctic. *Innovation* **5**, 100714 (2024).
51. Solomon, S. *Climate Change 2007-the Physical Science Basis: Working Group I Contribution To The Fourth Assessment Report Of The IPCC*. Vol. 4 (Cambridge university press, 2007).
52. Pederson, N., Hessl, A. E., Baatarbileg, N., Anchukaitis, K. J. & Di Cosmo, N. Pluvials, droughts, the Mongol Empire, and modern Mongolia. *Proc. Natl Acad. Sci. USA* **111**, 4375–4379 (2014).
53. Fang, Y. et al. Assessment of water storage change in China's lakes and reservoirs over the last three decades. *Remote Sens.* **11**, 1467 (2019).
54. Yao, F. et al. Satellites reveal widespread decline in global lake water storage. *Science* **380**, 743–749 (2023).
55. National Bureau of Statistics. *China Statistical Yearbook*. https://www.stats.gov.cn/sj/ndsj/ (2024).
56. Yu, Q. et al. A cultivated planet in 2010: 2. the global gridded agricultural production maps. *Earth Syst. Sci. Data Discus.***2020**, 1–40 (2020).
57. Qin, X., Wu, B., Zeng, H., Zhang, M. & Tian, F. Global gridded crop production dataset at 10 km resolution from 2010 to 2020. *Sci. Data* **11**, 1377 (2024).
58. Wu, H. et al. AsiaRiceYield4km: seasonal rice yield in Asia from 1995 to 2015. *Earth Syst. Sci. Data Discus.* **2022**, 1–30 (2022).
59. Arnell, N. W. Climate change and water resources in Britain. *Clim. Change* **39**, 83–110 (1998).
60. Wang, X., Xiao, X., Zhang, C., Dong, J. & Li, B. Effects of the 2022 extreme droughts on avian influenza transmission risk in Poyang Lake. *Innov. Life* **1**, 100044 (2023).
61. Forsee, W. J. & Ahmad, S. Evaluating urban storm-water infrastructure design in response to projected climate change. *J. Hydrol. Eng.* **16**, 865–873 (2011).
62. Kalra, A. & Ahmad, S. Evaluating changes and estimating seasonal precipitation for the Colorado River Basin using a stochastic nonparametric disaggregation technique. *Water Resour. Res.* https://doi.org/10.1029/2010WR009118 (2011).
63. Dawadi, S. & Ahmad, S. Evaluating the impact of demand-side management on water resources under changing climatic conditions and increasing population. *J. Environ. Manage.* **114**, 261–275 (2013).
64. Yi, S. & Sneeuw, N. Filling the data gaps within GRACE missions using singular spectrum analysis. *J. Geophys. Res. Solid Earth* **126**, e2020JB021227 (2021).
65. Abatzoglou, J. T., Dobrowski, S. Z., Parks, S. A. & Hegewisch, K. C. TerraClimate, a high-resolution global dataset of monthly climate and climatic water balance from 1958–2015. **5**, 1–12 (2018).
66. Lehner, B. et al. The Global Dam Watch database of river barrier and reservoir information for large-scale applications. *Sci. Data* **11**, 1069 (2024).
67. Earth Data. *Center for International Earth Science Information Network Gridded Population of the World Version 4 (GPWv4): Population Count*. https://sedac.ciesin.columbia.edu/data/collection/gpw-v4 (2024).
68. Wang, X. et al. Mapping coastal wetlands of China using time series landsat images in 2018 and google Earth engine. *ISPRS J. Photogr. Remote Sens.* **163**, 312–326 (2020).

69. Feng, M., Sexton, J. O., Channan, S. & Townshend, J. R. A global, high-resolution (30 m) inland water body dataset for 2000: First results of a topographic–spectral classification algorithm. *Int. J. Digital Earth* **9**, 113–133 (2016).
70. Stanimirova, R. et al. A global land cover training dataset from 1984 to 2020. *Sci. Data* **10**, 879 (2023).
71. Zhang, C. & Xiao, X. *Annual Yearlong Surface Water in Northeast Asia From 2000 to 2023*, https://doi.org/10.6084/m9.figshare.28848458.v1 (2025).

Acknowledgements

This study was in part supported by grants from the U.S. National Science Foundation (1911955, 2200310), the National Key Research and Development Program of China (2023YFF0806900), and the Natural Science Foundation of China (32330065). The publication fee was provided in part by the University of Oklahoma Libraries' Open Access Fund.

Author contributions

X.X. and C.Z. conceptualized the study. C.Z. carried out the data processing. C.Z. and X.X. led the result interpretation and manuscript writing. X.W., S.Y., C.M., Y.Q., Y.Y., and L.Y. contributed to the data processing. C.M., J.C., L.P., B.P., X.Y., and J.D. contributed to the result interpretation and discussion. All authors discussed and revised the paper.

Competing interests

The authors declare no competing interests.

Additional information

Supplementary information The online version contains supplementary material available at https://doi.org/10.1038/s43247-025-02449-0.

Correspondence and requests for materials should be addressed to Xiangming Xiao.

Peer review information *Communications Earth and Environment* thanks Nan Xu, and Chao Wang for their contribution to the peer review of this work. Primary Handling Editor: Alireza Bahadori. A peer review file is available.